Synergistically enhancing the selective adsorption for crystal planes to regulate the (002)-texture preferred Zn deposition via supramolecular host-guest units

Lequan Wang[§1], Yizhen shao[§1,6]hongheng Fu[§3], Xianfu Zhang[2], Junming Kang[1], Xingxiu Yang[1], Zhimin Zhai[1], Ying Ge[1], Long Zhang[2], Yanglong Hou[2,5]*, and Hongbin Lu[1,4]**

[1]State Key Laboratory of Molecular Engineering of Polymers, Department of Macromolecular Science, Fudan University, Shanghai 200438, China

[2]School of Materials, Shenzhen Campus of Sun Yat-sen University, Shenzhen, Guangdong 518107, China

[3]Beijing Advanced Innovation Center for Materials Genome Engineering, Institute for Advanced Materials and Technology, University of Science and Technology Beijing, Beijing 100083, China

[4]Yiwu Research Institute of Fudan University, Yiwu City, Zhejiang 322000, China

[5]School of Materials Science and Engineering, Beijing Key Laboratory for Magnetoelectric Materials and Devices, Peking University, Beijing 100871, China

[6]Faculty of Materials Science and Energy Engineering, Shenzhen University of Advanced Technology, Shenzhen, Guangdong 18107 China

[§]These authors contributed equally to this work.

[*]Corresponding authors: Long Zhang (L.Z); Yanglong Hou (Y.H.); Hongbin Lu (H.L.).

E-mail addresses: zhanglong25@mail.sysu.edu.cn; hou@pku.edu.cn; hongbinlu@fudan.edu.cn.

1. Experimental Section

1.1 Preparation of SDCD@Zn

Firstly, aqueous solution of 0.07 M β-CD (Aladdin) and 0.028 M SDBS (Aladdin) were mixed with stirring. The obtained mixture was then heated to 80 °C to obtain a clear and homogeneous solution. Finally, the solution was cooled to room temperature at 25 °C and after approximately 6 h an equilibrium state was reached by forming SDCD supramolecular complex units. The SDCD@Zn anode was prepared by blade coating the as-formed SDCD dispersion onto the polished Zn foil surface by using a 10 μm blade gap and then dried naturally. All chemicals were used without further purification.

1.2 Material Characterizations

Field-emission scanning electron microscopy (FESEM) images were acquired from a Zeiss Ultra55, equipped with an Aztec XMax Extreme energy dispersive spectrometer (EDS). Fourier transform infrared (FTIR) spectra were collected on a Thermofisher Nicolet iS50 spectrometer. X-ray photoelectron spectroscopy (XPS) measurements were carried out with a PHI Genesis 500 (ULVAC-PHI) under vacuum. X-ray diffraction (XRD) patterns and corresponding pole figure data were measured by Rigaku Smatlab 9KW. High-resolution transmission electron microscope (HRTEM) images were collected from a JEM-2010F transmission electron microscope. Atomic force microscopy (AFM) data were acquired from a Cypher VRS1250 (Oxford). Electron backscattered diffraction (EBSD) images were collected from a scanning electron microscopy with EDAX-TSL system. In situ Zn deposition processes were observed using an optical microscope (Motic-BA310Met).

1.3 Electrochemical tests

For the performance evaluation of bare Zn and SDCD@Zn anodes, Zn/Zn symmetric cells and Zn/Cu asymmetric cells were used for cycle tests, using 2 M $ZnSO_4$ as the aqueous electrolyte and GF/D glass fiber as the separator. The MnO_2 cathode was prepared as follows: the active material was mixed with carbon black and polytetrafluoroethylene (PTFE) in a mass ratio of 7:2:1. The mixture was then compressed onto a metallic Ti grid. The electrode was dried under vacuum at 80 °C for 12 h and then punched into discs. All batteries were tested for electrochemical performance using 2016-coin cells. All galvanostatic charge-discharge tests were performed using a battery tester (Land CT2001A).

Electrochemical impedance spectroscopy (EIS), cyclic voltammetry (CV), linear polarization curves, linear sweep voltammetry (LSV), chronoamperograms (CA) data were performed by a CHI 660E electrochemical workstation. The linear polarization curves were obtained by scanning between −0.94 and −1.1 V at 5 mV s^{-1} with Zn plate as the working electrode, Pt wire as the counter electrode, and SCE as the reference electrode in 2 M $ZnSO_4$ solution. LSV curves were accomplished at a scan rate of 5 mV s^{-1} in 2 M Na_2SO_4 solution. CA measurement was conducted on SDCD@Zn and bare Zn at −200 mV in 2 M $ZnSO_4$ solution. The CV test of the Zn/Cu asymmetric cell was carried out at a scan rate of 1 mV s^{-1}. CV curves of the Zn/MnO_2 full cell were

recorded over a voltage range of 0.6-1.85 V. EIS was tested at open circuit potential with a frequency in the range of 100 kHz to 0.1 Hz and an amplitude of 5 mV. Zview software was used to analyze the equivalent circuit and fitting parameters of the impedance data. Differential capacitance curves were obtained from equation $C=-(\omega Z_{im})^{-1}$, where C, ω, and Z_{im} represent differential capacitance, angular frequency, and imaginary part of impedance, respectively. To avoid the influence of Zn^{2+} deposition behavior, Na_2SO_4 solution was selected as the test solution. The E_a can be extracted from the fitting of the Arrhenius equation: $\frac{1}{R_{ct}} = Ae^{\frac{-E_a}{RT}}$, where A is the pre-exponential factor, T is the absolute temperature (K), and R_{ct} and R represent the charge transfer resistance and standard gas constant (8.314 J mol^{-1} K^{-1}), respectively.

1.4 Density functional theory (DFT) calculations

The first-principles tool, Vienna Ab initio Simulation Package(VASP), was employed to carry out all DFT calculations within the generalized gradient approximation (GGA) via the Perdew-Burke-Ernzerhof (PBE) formulation. We have selected the projected augmented wave (PAW) potentials to describe the ionic cores and taken valence electrons into account using a plane wave basis set with a kinetic energy cutoff of 450 eV. Partial occupancies of the Kohn−Sham orbitals were allowed using the Gaussian smearing method and a width of 0.05 eV. For optimizing both geometry and lattice size, the Brillouin zone integration was carried out with 1×1×1 *Γ*-centered *k*-point sampling. The self-consistent calculations adopted a convergence energy threshold of 10^{-5} eV. The equilibrium geometries and lattice constants were optimized with maximum stress on each atom within 0.02 eV $Å^{-1}$. The 35 Å vacuum layer was typically added to the surface to preclude the artificial interactions between periodic images and to loaded the adsorbent molecule. The weak interaction was depicted by DFT+D3 method with empirical correction in Grimme's scheme. Spin polarization method was adopted to describe the magnetic system. Moreover, the input files and output data of electrostatic potential and charge difference were generated by the Vaspkit tool. The IGM analysis was calculated by the Multiwfn tool. The adsorption energy was computed as: E_{ads} = E(*adsorbent) - E(*) - E(adsorbent). E(*adsorbent), E(*) and E(adsorbent) represent the total energy of *adsorbent, *, and adsorbent molecule, respectively.

1.5 Molecular dynamics (MD) simulations

The partial charge of SO_4^{2-}, adsorbed molecule was calculated using Gaussian 16 code and the 6-311g(d,p) basis functions were applied. The OPLS-AA force field and Auxiliary Tools of Force Field（AuToFF）were used to parametrize all atoms, such as the bond parameters, angle parameters and dihedral angles. The parameters of SO_4^{2-} were derived from OPLS-2009IL force field. The Zn crystals were sliced, and Zn electrode adopted (101) crystal face.

Firstly, the adsorption model of adsorption molecules was constructed, that is, the adsorption molecules were arranged in a structure similar to phospholipid bilayer, and then placed on the Zn substrate. The kinetic equilibrium simulation was performed for 1 ns in the NPT ensemble, and then for 20 ns in the NVT ensemble to obtain a stable adsorption substrate model. 2 M $ZnSO_4$ aqueous solution (composed of 200 $ZnSO_4$ and 5560 water molecules) was then randomly placed on top of the adsorption substrate model, and the lower Zn substrate was fixed to keep the structure

unchanged. The adsorption simulation was processed in an NVT ensemble and the simulation time was 20 ns.

The MD simulations were performed in the GROMACS 2021 software package. The steepest descent method was applied to minimize the initial energy for each system with a force tolerance of 1 kJ (mol^{-1} nm^{-1}) and a maximum step size of 0.002 ps before MD calculations. In all the three directions, periodic boundary conditions were imposed. Leapfrog algorithm was used to integrate the Newtonian equation of motion. In NVT simulations, the temperature was maintained by the V-rescale thermostat at 298.15 K. A cutoff of 1.2 nm was employed to calculate the short-range van der Waals interactions and electrostatic interactions.

In NPT simulations, the pressure was maintained at 1 bar by the Berendsen barostat in an anisotropic manner. The temperature was maintained by the V-rescale thermostat at 298.15 K.

2. Supplementary Characterization

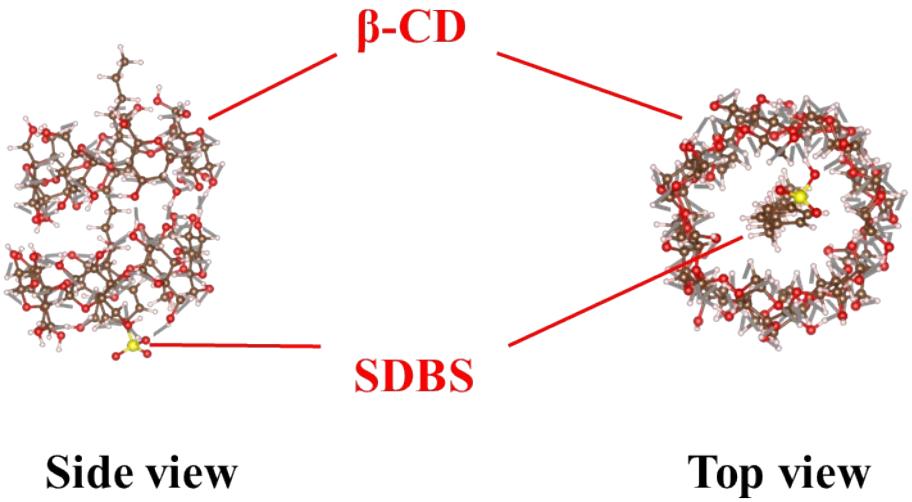

Figure S1. Top view and side view of the supramolecular complex unit.

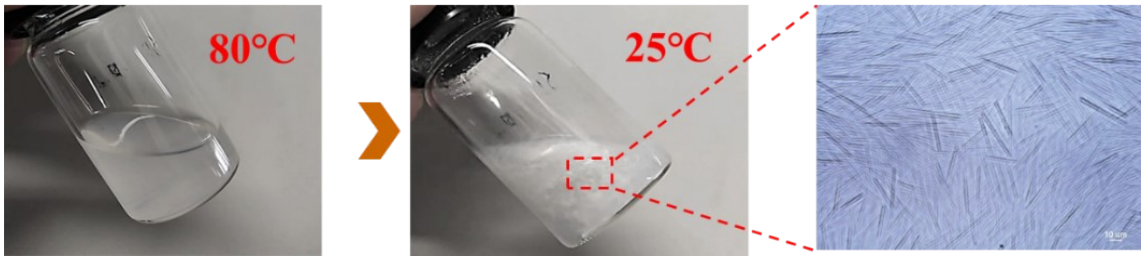

Figure S2. Solution states of supramolecular complex units at 25 °C and 80 °C, and corresponding self-assembled microstructures.

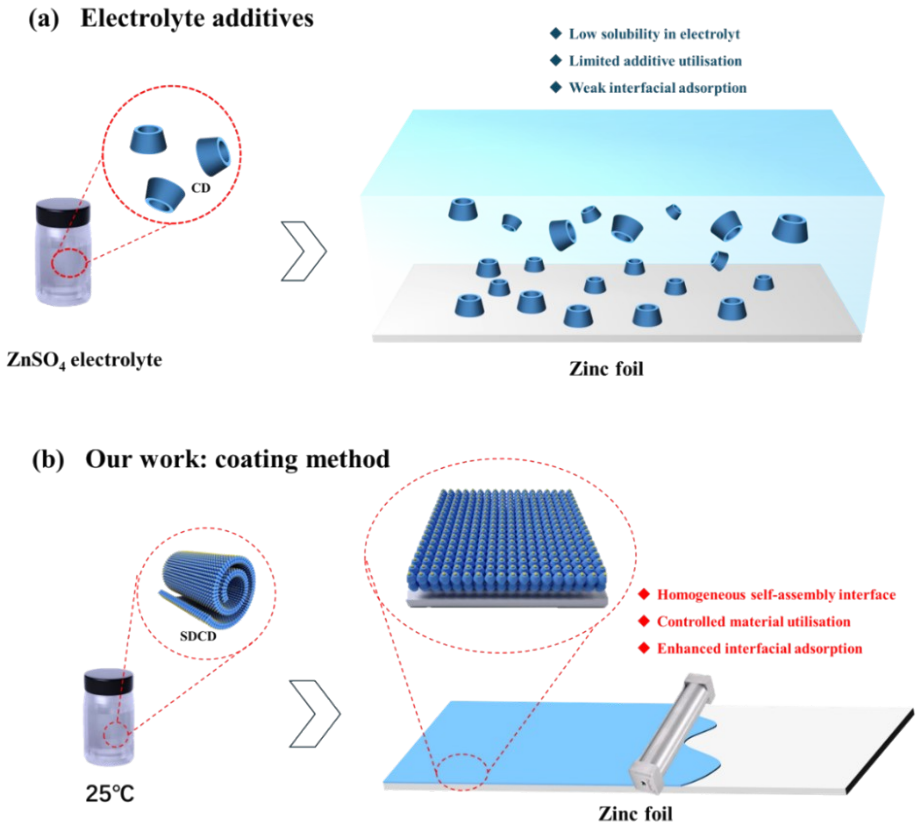

Figure S3. Comparison of CDs in aqueous Zn metal batteries in terms of usage method: (a) electrolyte additive and (b) interface engineering.

Most previous studies introduced CDs into battery systems as electrolyte additives. As shown in Figure S3a, the limited solubility of CDs in electrolytes significantly restricts their application as additives. Additionally, the large number of free CDs in the electrolyte and the relatively weak interfacial adsorption capacity between CDs and Zn result in only a small number of CDs being adsorbed on the Zn surface. In our work, we adopted a scalable doctor-blade method to uniformly and controllably coat host-guest complex units containing CDs directly onto the Zn foil surface. This approach not only allows precise control of CD dosage but also ensures that CDs can stably and efficiently function on the Zn surface over the long term. (Figure S3b).

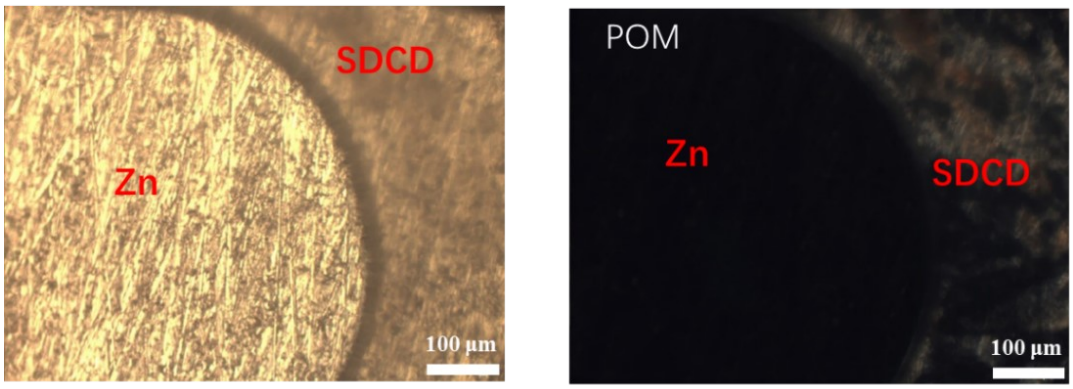

Figure S4. Optical microscope image (left) and POM image (right) of Zn surface with SDCD aqueous solution.

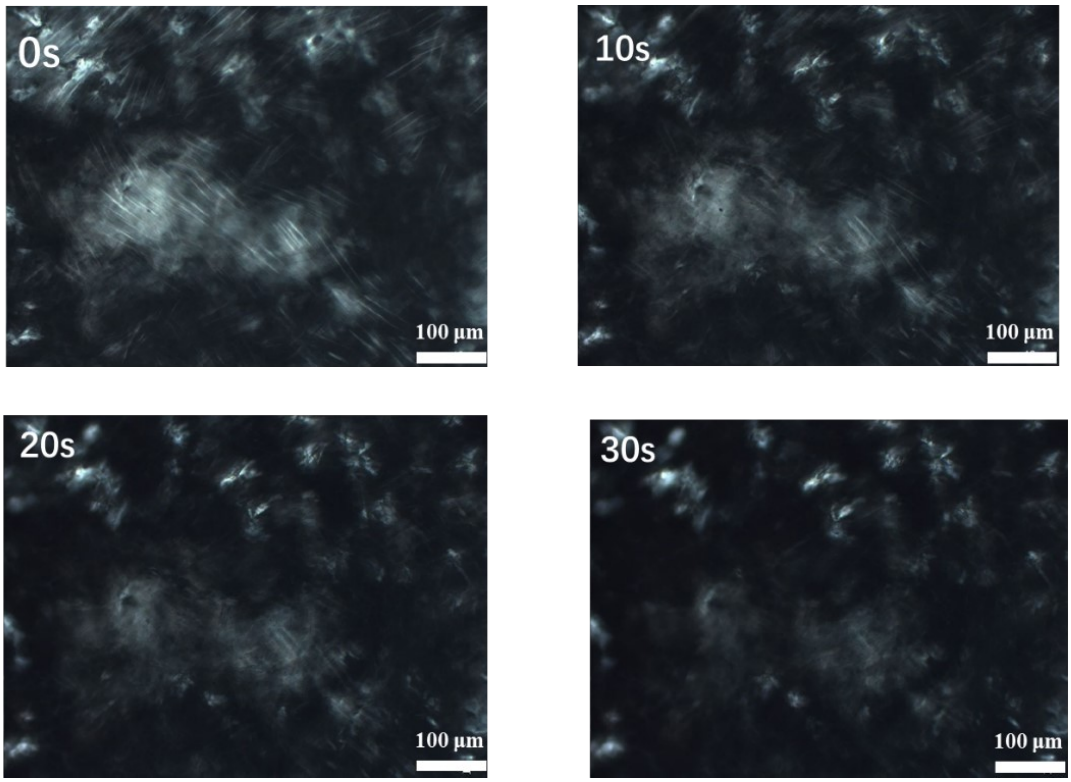

Figure S5. POM images of the evolution of SDCD assembly micelles over time in the presence of Zn substrate.

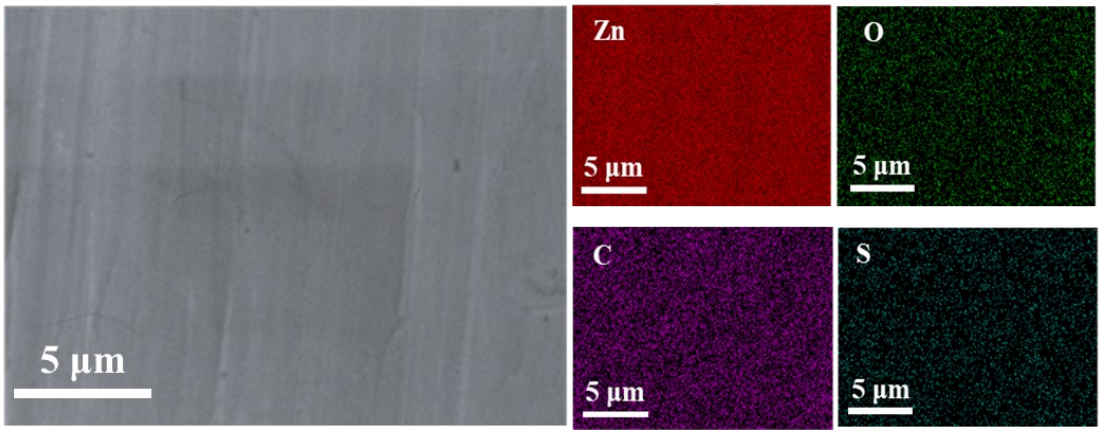

Figure S6. SEM image and corresponding element mappings of SDCD@Zn.

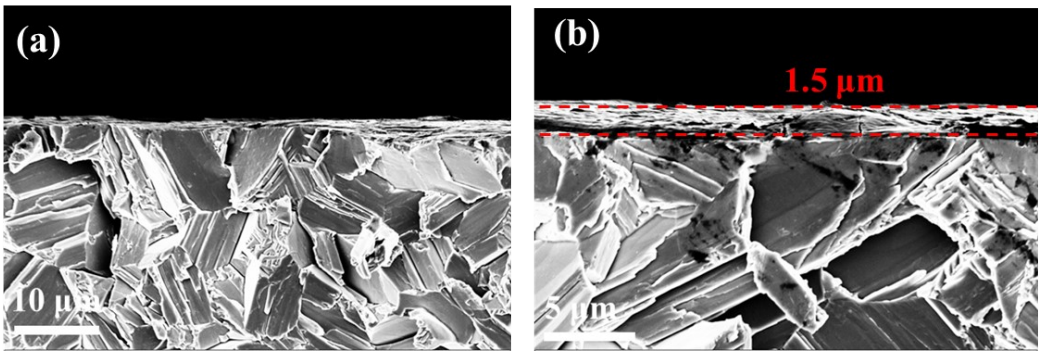

Figure S7. Cross-sectional SEM images of the SDCD@Zn electrode.

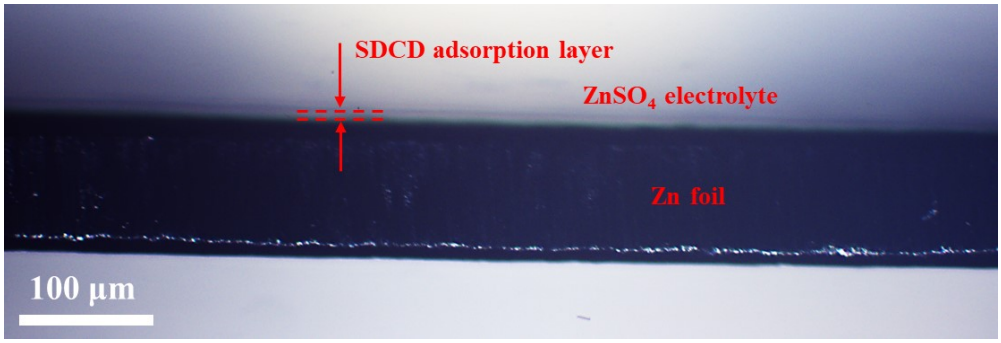

Figure S8. Optical photograph of SDCD adsorption layer on the surface of Zn foil in the electrolyte.

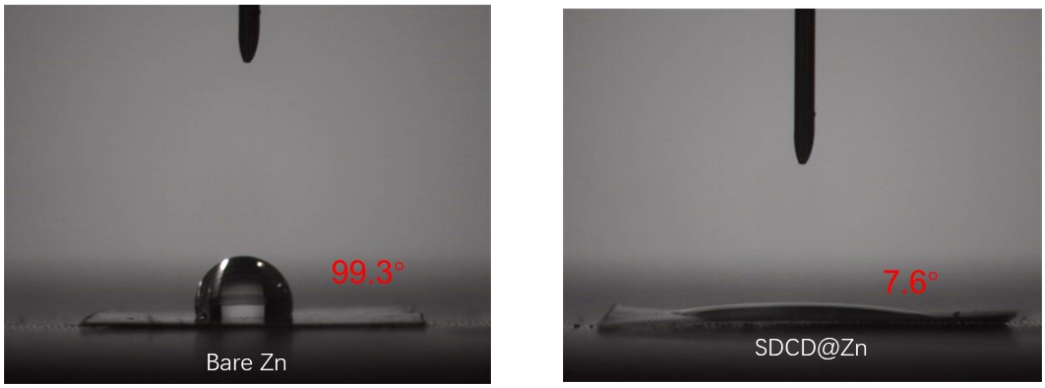

Figure S9. Contact angle test of bare Zn and SDCD@Zn.

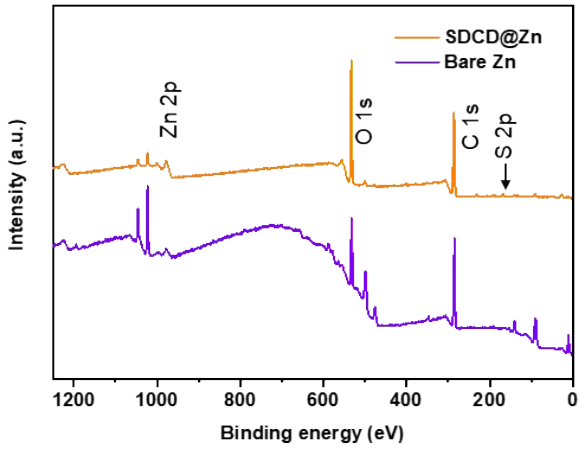

Figure S10. XPS spectra of bare Zn and SDCD@Zn electrodes.

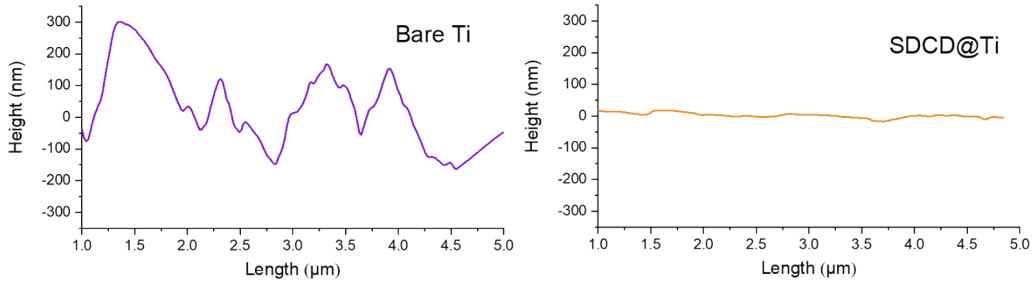

Figure S11. AFM height profiles of Zn deposits of 0.1mAh cm^{-2} on bare Ti and SDCD@Ti.

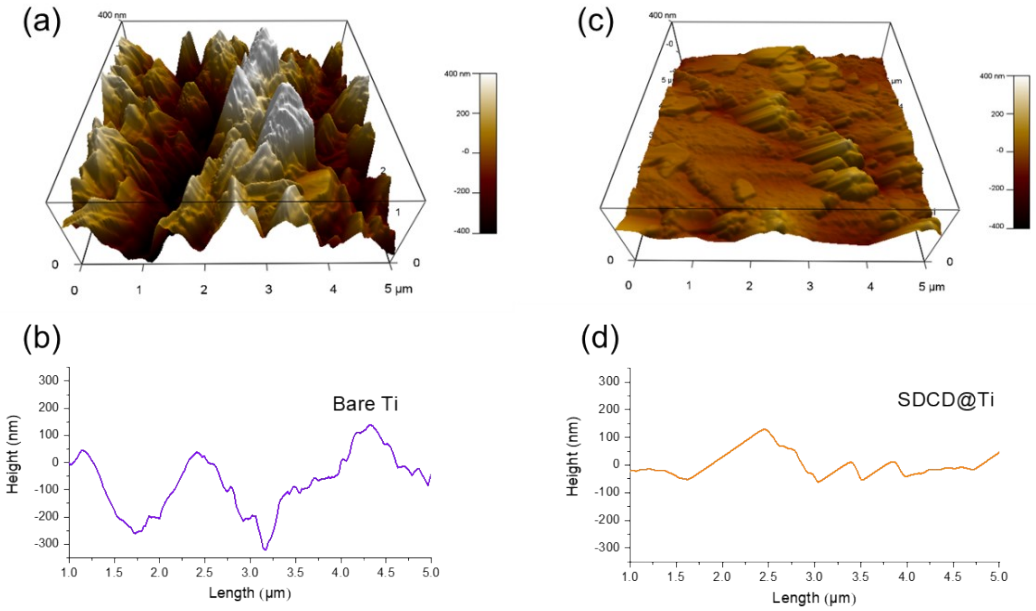

Figure S12. AFM 3D height images and corresponding height profiles of Zn deposits of 0.5 mAh cm^{-2} on (a, b) Ti foil and (c, d) SDCD@Ti.

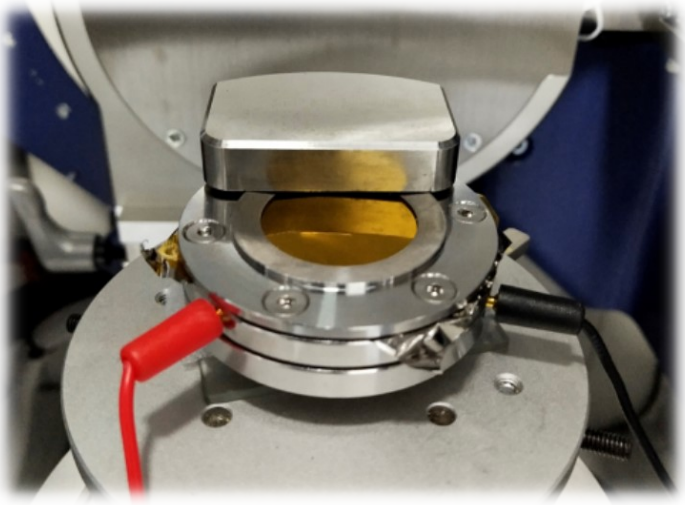

Figure S13. Self-fabricated test setup for in situ XRD.

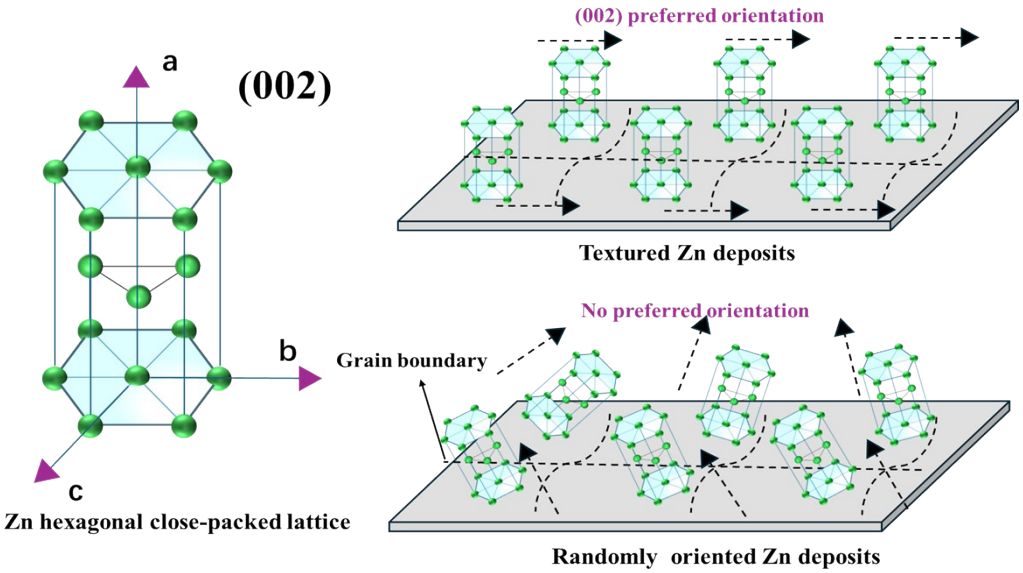

Figure S14. Schematic illustration of Zn(002)-crystal plane preferred orientation.

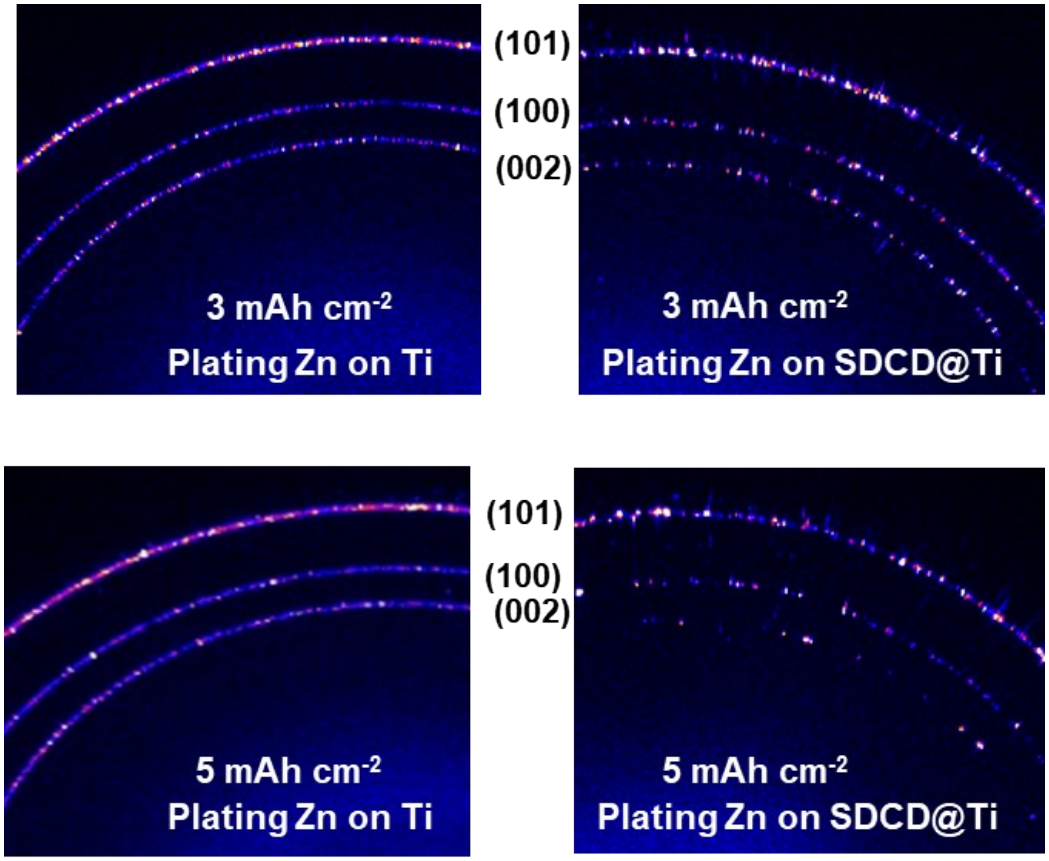

Figure S15. 2D XRD results of plating Zn on bare Ti foil (left) and SDCD@Ti (right).

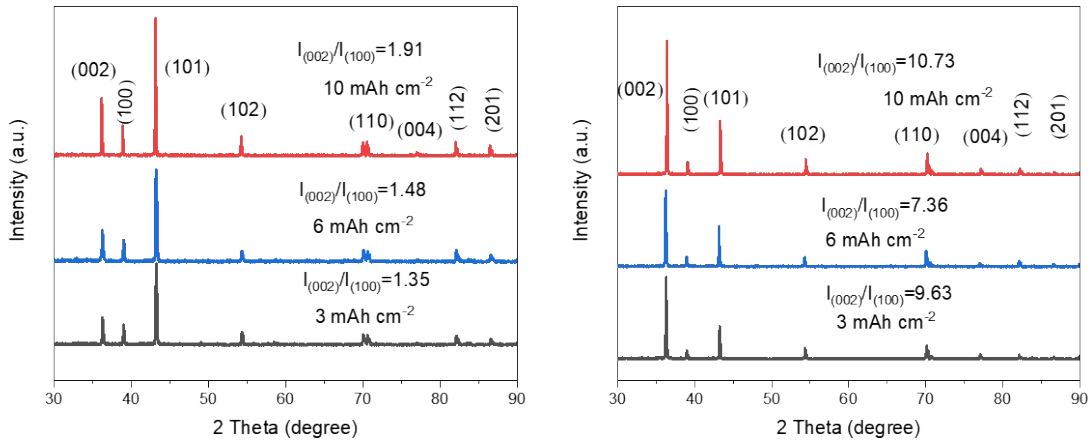

Figure S16. 1D XRD results of plating Zn on bare Ti foil (left) and SDCD@Ti (right).

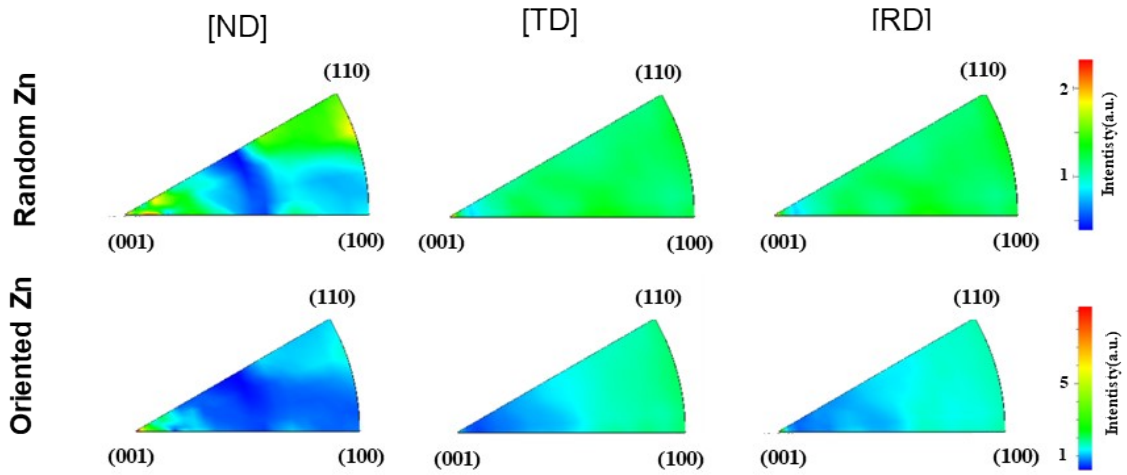

Figure S17. Inverse pole figures of the Zn deposits on bare Ti (up) and SDCD@Ti (down).

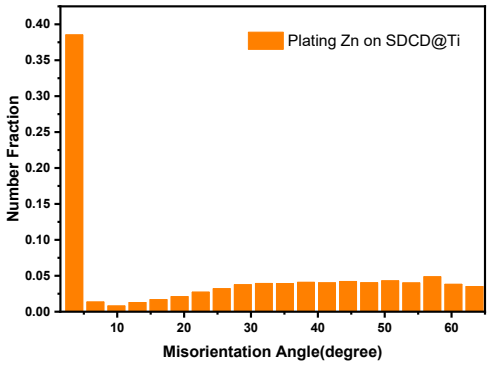

Figure S18. Misorientation angle distribution plot of Zn deposition on SDCD@Ti.

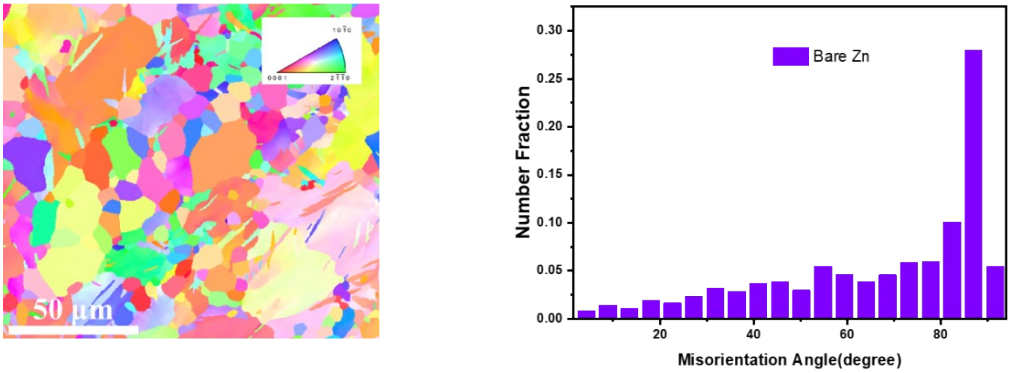

Figure S19. EBSD distribution map (left) and misorientation angle distribution plot (right) of bare Zn.

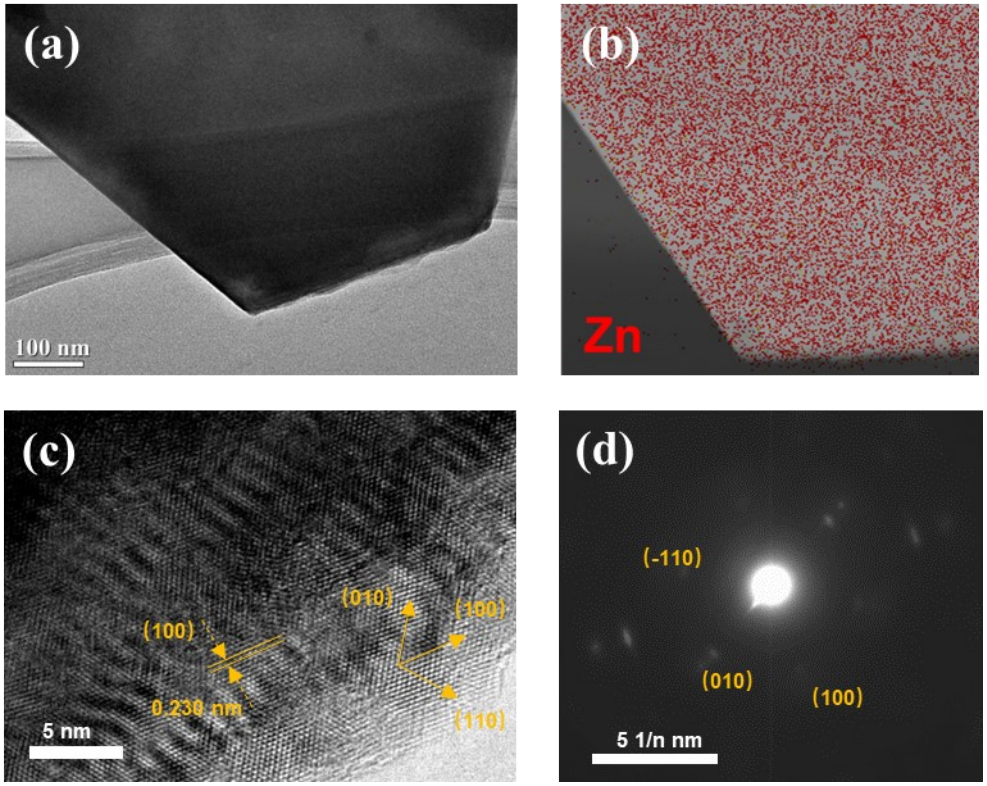

Figure S20. HRTEM images, corresponding element mapping and SAED patterns of the Zn sheet deposited on SDCD@Ti.

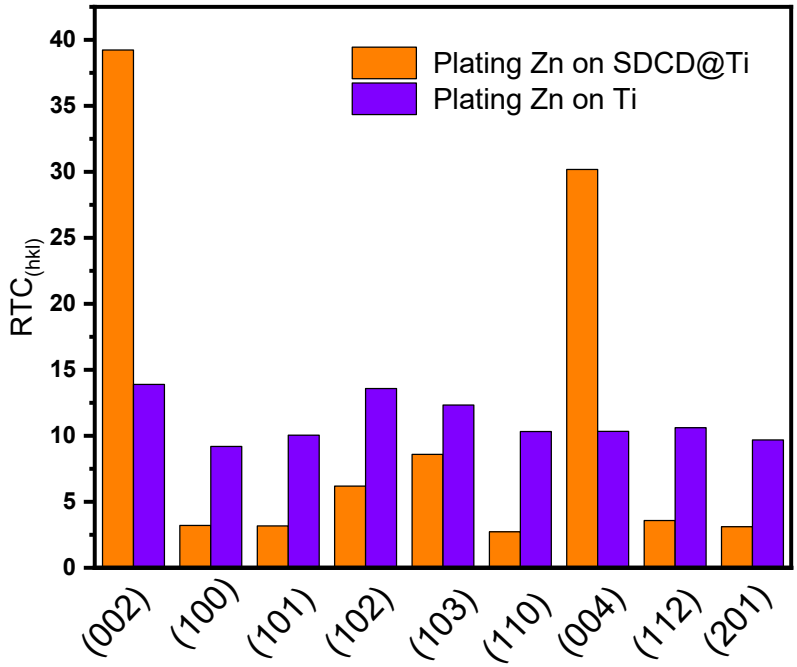

Figure S21. Calculated RTCs of different Zn crystal planes.

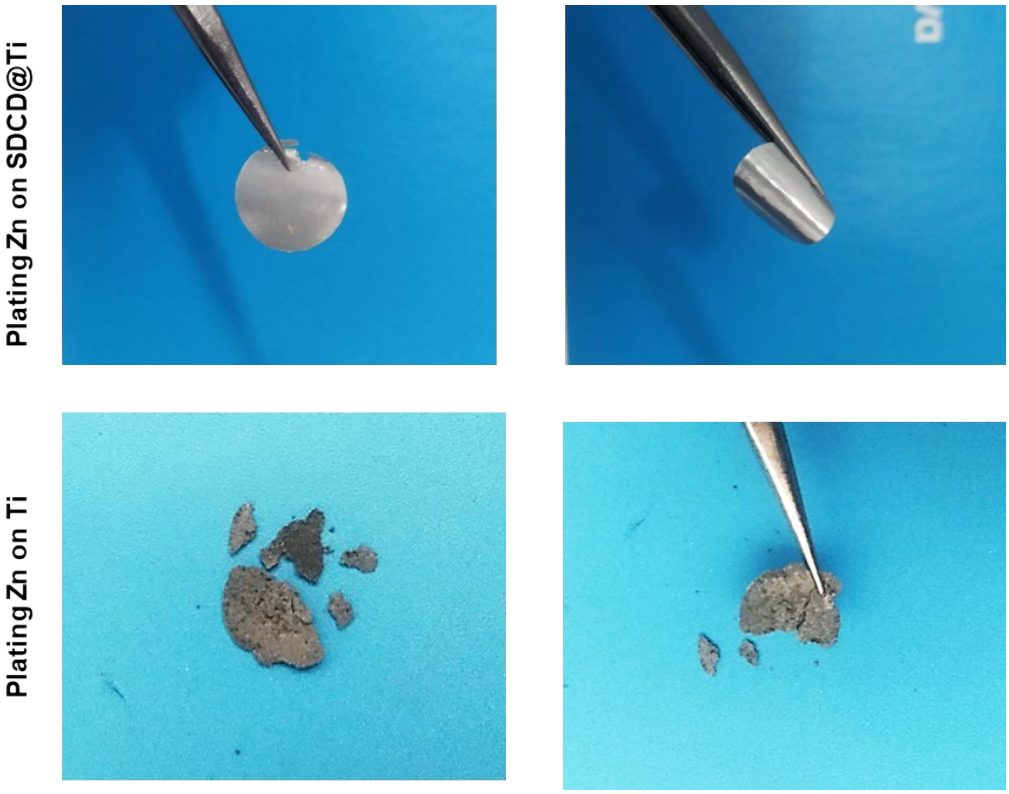

Figure S22. The deposited Zn layer of 10 mAh cm^{-2} on bare Ti and SDCD@Ti.

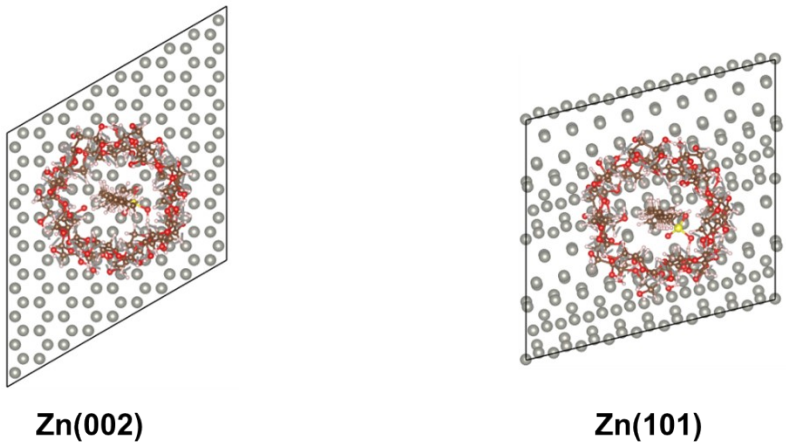

Figure S23. Top view of the adsorption models of SDCD on the Zn(002) and Zn(101) crystal planes.

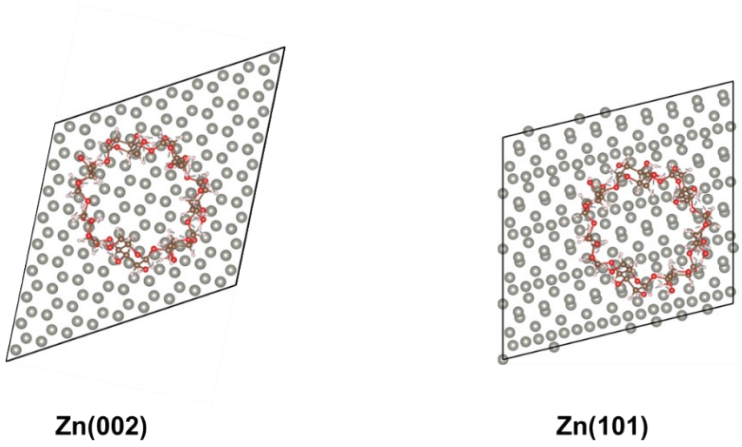

Figure S24. Top view of the adsorption models of β-CD on the Zn(002) and Zn(101) crystal planes.

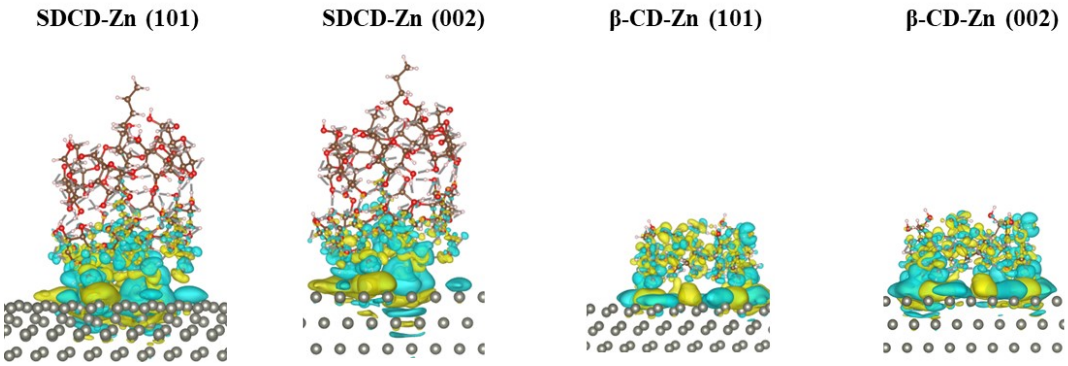

Figure S25. Charge density difference of the Zn (002) and Zn (101) crystal planes with SDCD and β-CD molecules.

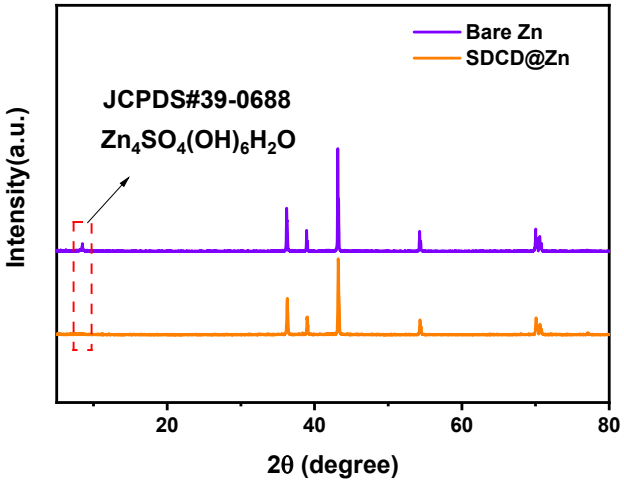

Figure S26. XRD patterns of bare Zn and SDCD@Zn after immersion in electrolyte for 24 h.

Figure S27. Graphs of the cell thickness results with SDCD@Zn (left) and bare Zn (right) anodes after cycling (Insets show tested cell).

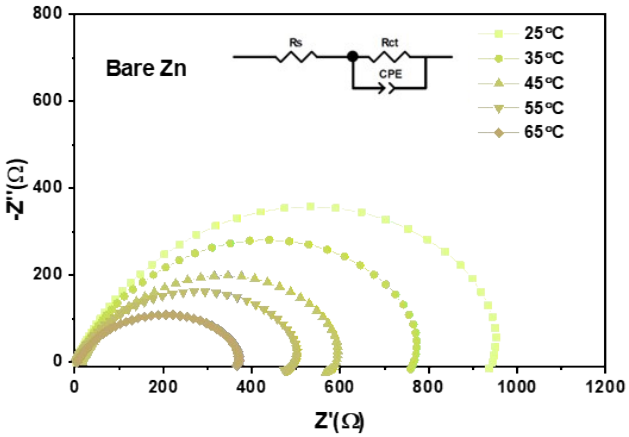

Figure S28. Nyquist plots of the Zn/Zn cells at different temperatures.

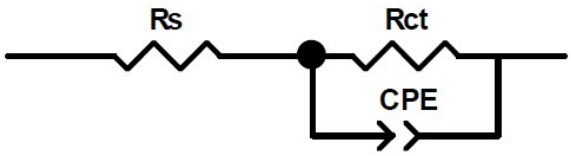

Figure S29. An equivalent circuit is used to simulate the resistances of bare Zn symmetric cell, where R_s is the ohmic resistance, R_{ct} is the charge transfer resistance, CPE_1 is the double-layer capacitance.

Table S1. The fitting results of EIS plots of bare Zn samples.

Samples	R_s	R_{ct}
Bare Zn (25℃)	1.77	966.2
Bare Zn (35℃)	4.73	779.8
Bare Zn (45℃)	14.8	591.6
Bare Zn (55℃)	2.656	502.1
Bare Zn (65℃)	4.8	372.7

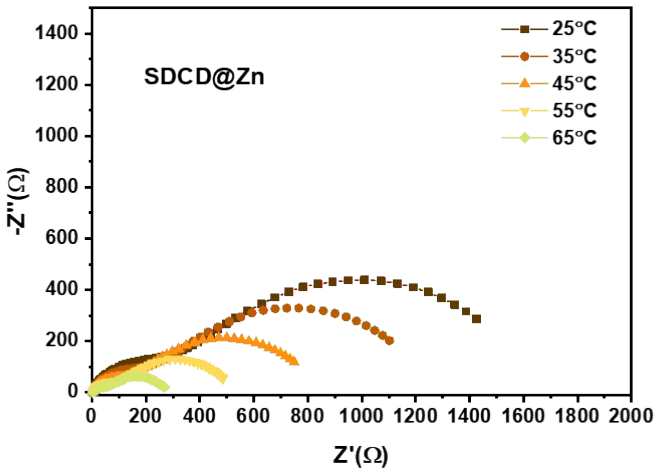

Figure S30. Nyquist plots of the SDCD@Zn symmetric cell at different temperatures.

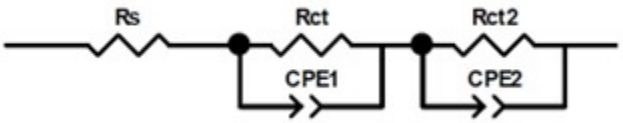

Figure S31. An equivalent circuit is used to simulate the resistances of the SDCD@Zn symmetric cell, where R_s is the ohmic resistance, R_{ct} and R_{ct2} are the charge transfer resistance, CPE_1 and CPE_2 are the double-layer capacitance, and W_1 is the Warburg impedance.

Table S2. The fitting results of EIS plots of SDCD@Zn samples.

Samples	R_s	R_{ct}	$R_{ct}2$
SDCD@Zn (25°C)	2.69	232.5	1398
SDCD@Zn (35°C)	2.75	173.4	1074
SDCD@Zn (45°C)	1.94	112.9	720.1
SDCD@Zn (55°C)	3.16	40.54	448.1
SDCD@Zn (65°C)	3.74	44.96	238.2

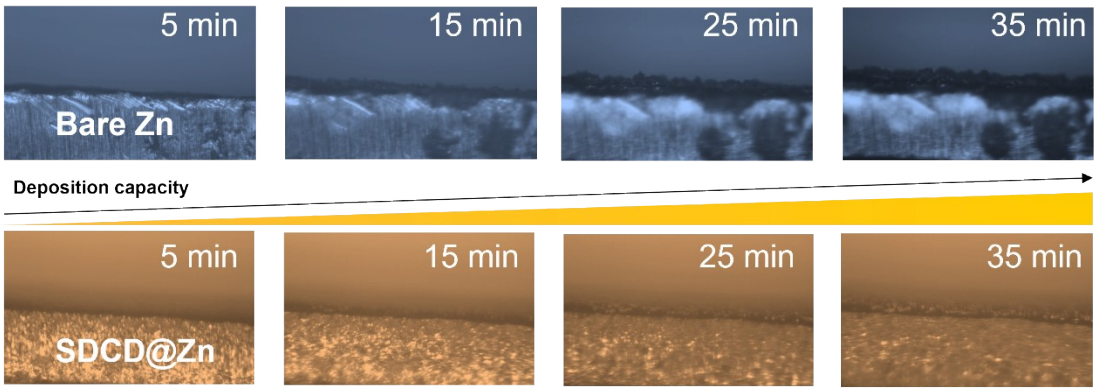

Figure S32. In situ optical observation of Zn deposition on bare Zn and SDCD@Zn in 2 M $ZnSO_4$ electrolyte.

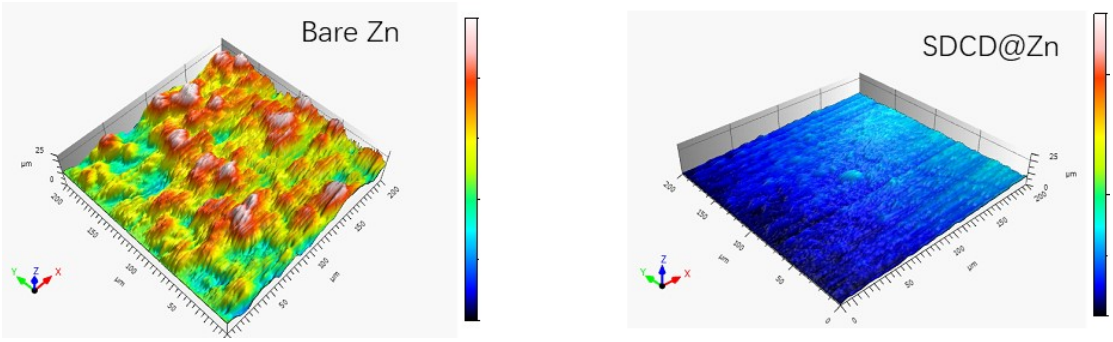

Figure S33. Three-dimensional contours of Zn deposition morphology on bare Zn (left) and SDCD@Zn (right).

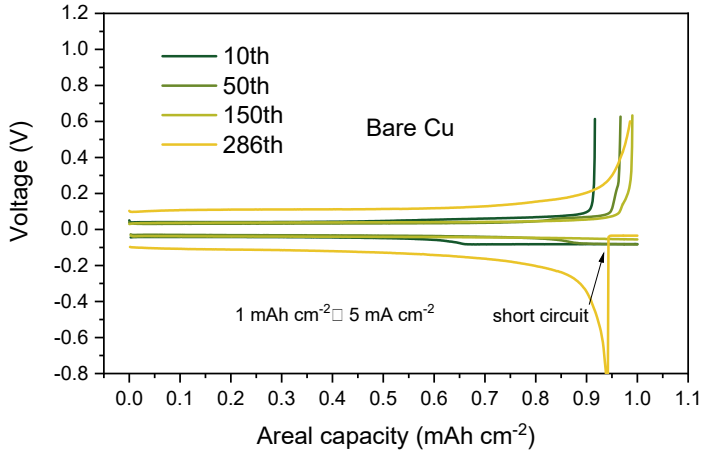

Figure S34. Voltage/capacity curves of Cu/Zn cells with bare Cu.

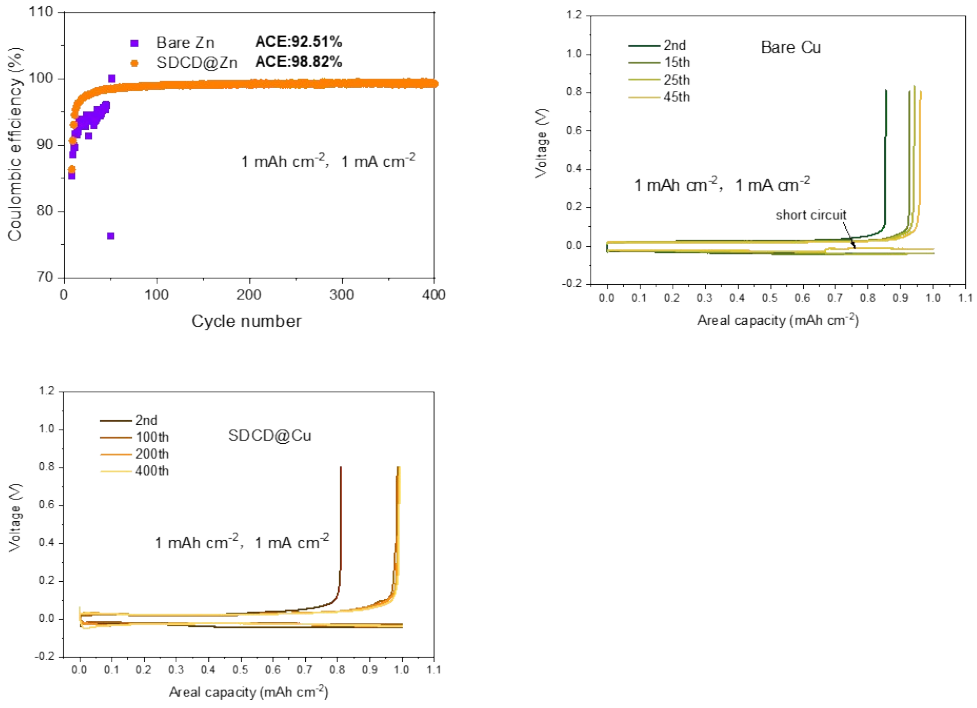

Figure S35. Zn plating/stripping tests of Cu/Zn cells with or without SDCD, and the corresponding voltage/capacity curves.

Table S3. A comparison of the key electrochemical performance of this work with previously reported works using cyclodextrins.

Ref.	current density (mA cm^{-2})	Areal capacity (mAh cm^{-2})	Cumulative cycling time (h)	Cumulative plating capacity (mAh cm^{-2})
1	1	1	1000	500
	5	5	350	875
2	4	2	1700	3400
3	10	1 (DOD 6%)	160	800
	5	5 (DOD 30%)	200	500
4	1	1	1600	800
5	5	5	300	750
6	10	10	600	3000
7	5	5	900	2250
	10	1	500	2500
8	5	2 (DOD 6.8%)	940	2350
9	2	1	3900	3900
	10	3	1035	5175
This work	**10**	**1** (DOD 1.7%)	**5800**	**29000**
	10	**10** (DOD 17%)	**900**	**4500**
	5.85	**5.85** (DOD 50%)	**260**	**761**

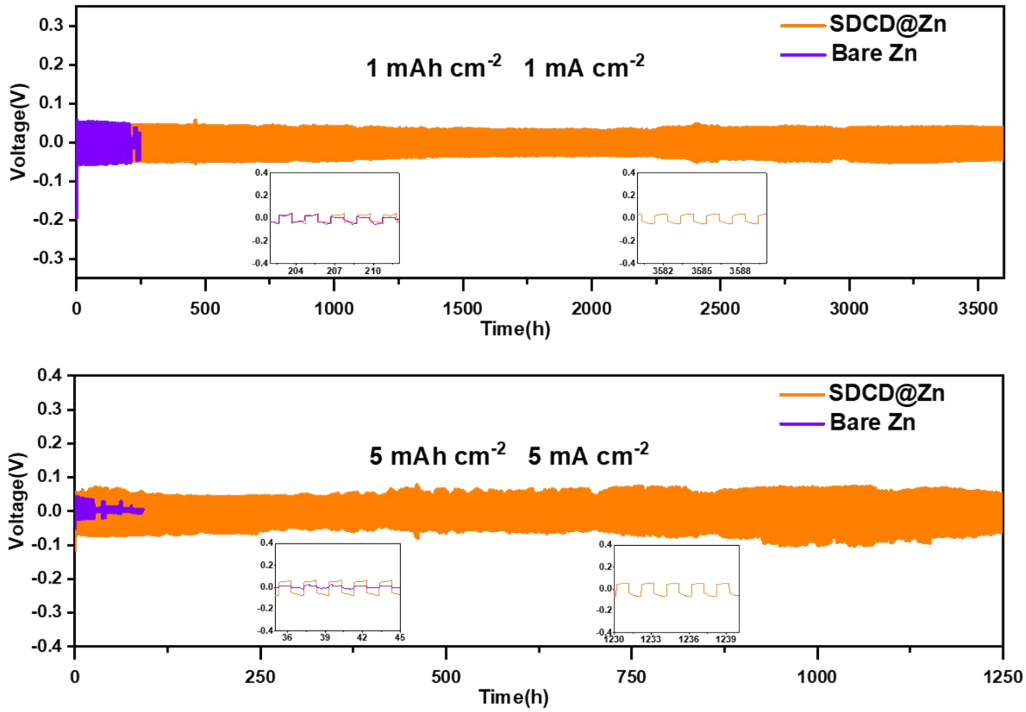

Figure S36 Cycling performance of Zn/Zn symmetric cells with or without SDCD. (Insets show the enlarged voltage-time curves).

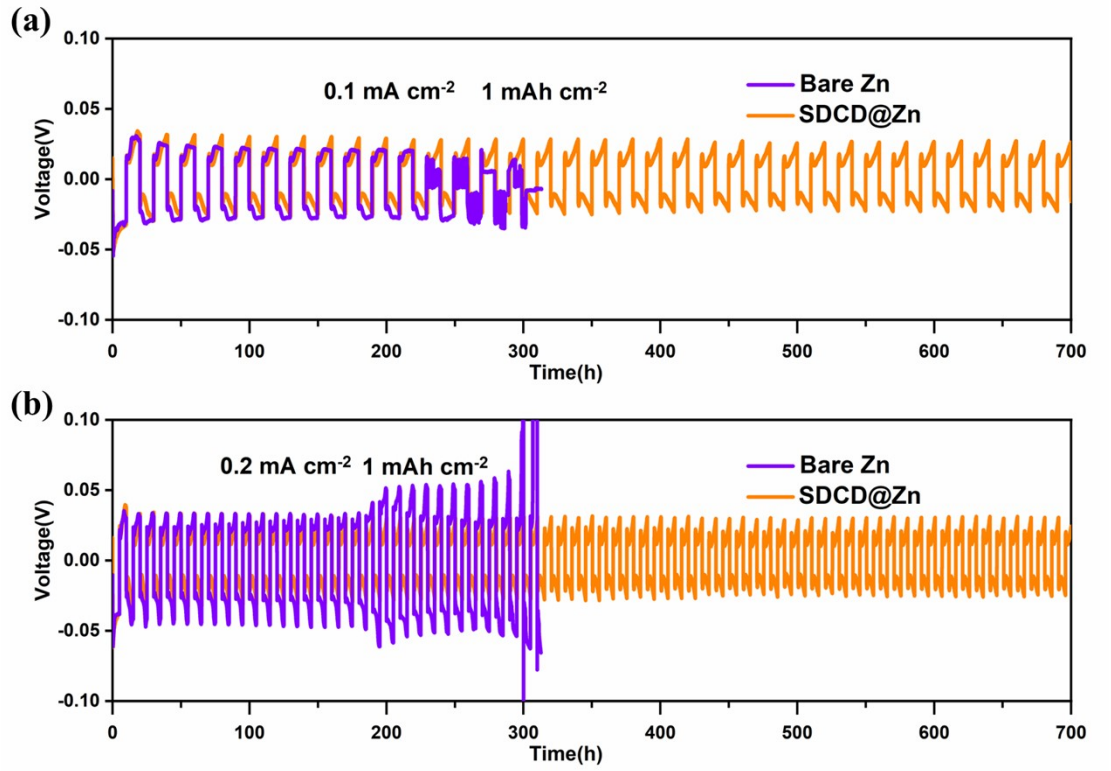

Figure S37. Cycling performance of Zn/Zn symmetric cells assembled with or without SDCD at (a) 0.1 mA cm^{-2} and (b) 0.2 mA cm^{-2} with areal capacity of 1 mAh cm^{-2}.

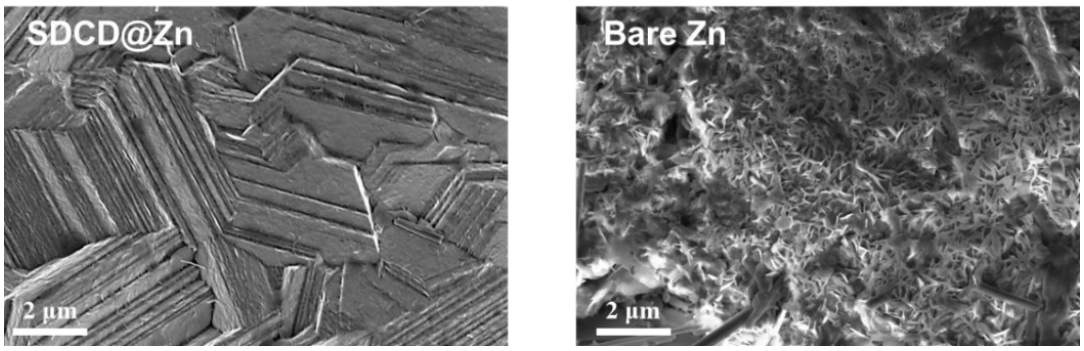

Figure S38. Top-view SEM images of Zn deposition morphology on SDCD@Zn (left) and bare Zn (right).

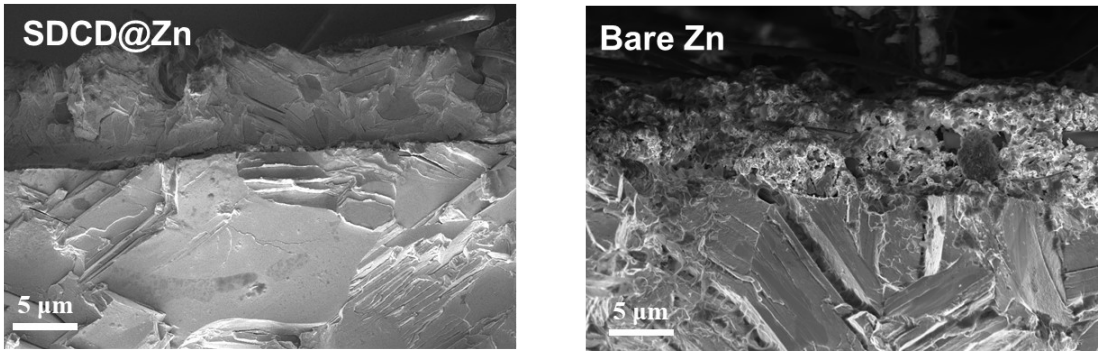

Figure S39. Cross-sectional SEM images of Zn deposition morphology on SDCD@Zn (left) and bare Zn (right).

Table S4. Comparison of performance of Zn/Zn symmetric cells enduring alternate cycling and resting process for this work with recently reported Zn-based cells.

Anode strategy	**current density (mA cm^{-2})**	**Areal capacity (mAh cm^{-2})**	**Cumulative cycling time (h)**	**Cumulative resting time (h)**	**Ref.**
Cu/Zn	1	0.5	360	288	10
$(C_2F_4)_n$-C@Cu@Zn	1	1	300	350	11
SG/ZSO	1	1	500	500	12
ZVO	1	0.5	500	500	13
HA gel	1	1	650	650	14
DME	2	2	600	600	15
MTSi-Zn	1	1	280	120	16
PCZ-gel	2	2	500	500	17
CMC	1	1	204	96	18
SAM	1	0.5	1400	300	19
FEC	1	1	528	72	20
MXene10^Zn	5	5	472	528	21
P-PFL@Zn	1	1	468	432	22
SDCD@Zn	**1**	**1**	**1750**	**1750**	***This work***

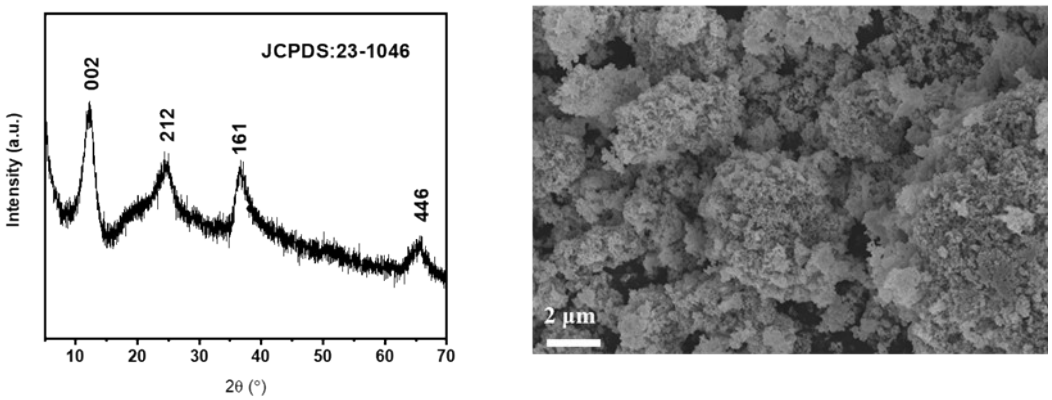

Figure S40. XRD pattern (left) and SEM image (right) of the prepared MnO_2.

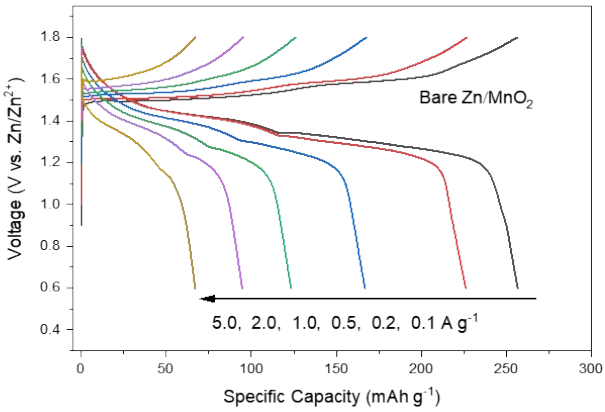

Figure S41. Charge/discharge curves of the bare Zn/MnO_2 full cell at different current densities.

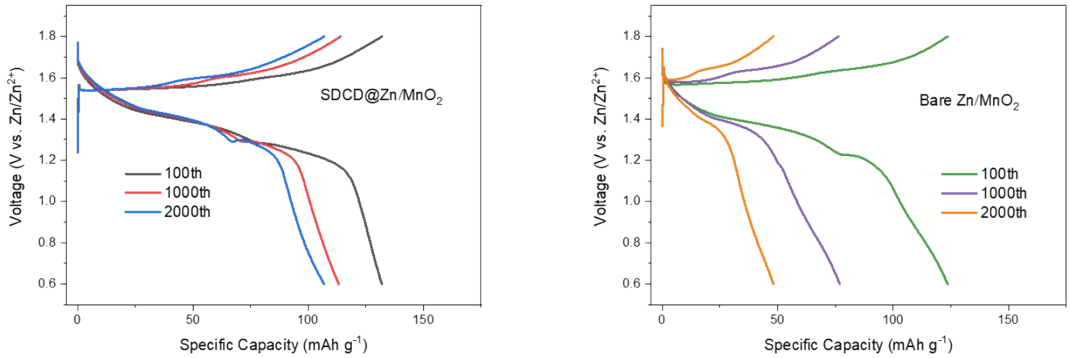

Figure S42. Charge/discharge curves of full cells in different cycles.

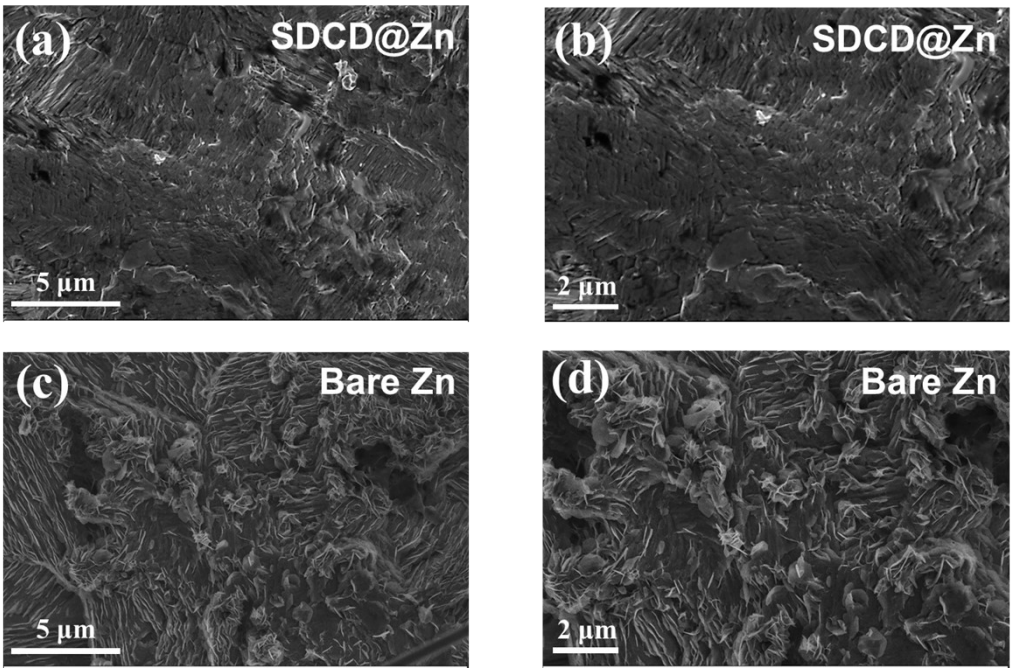

Figure S43. Surface morphologies of the SDCD@Zn and bare Zn anodes for Zn/MnO_2 full cells after 100 cycles.

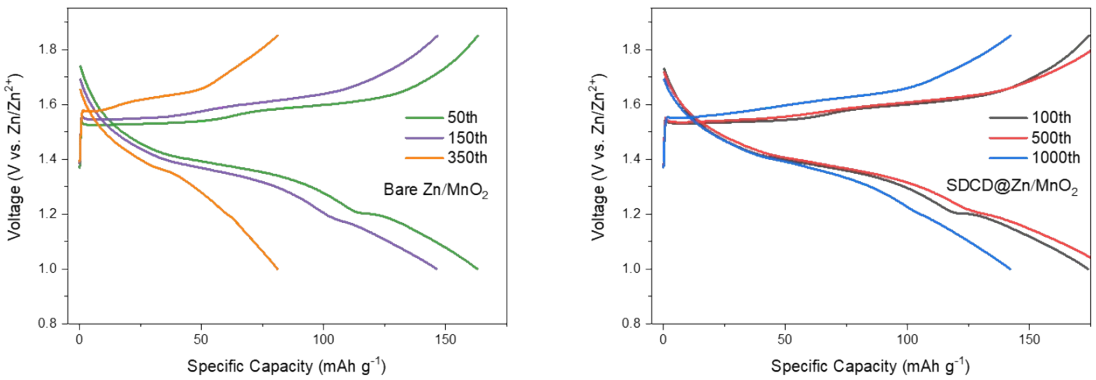

Figure S44. Charge/discharge curves of pouch cells in different cycles.

References

1. M. Qiu, P. Sun, Y. Wang, L. Ma, C. Zhi and W. Mai, *Angew. Chem. Int. Ed.*, 2022, **61**, e202210979.
2. C. Meng, W. He, L. Jiang, Y. Huang, J. Zhang, H. Liu and J.-J. Wang, *Adv. Funct. Mater.*, 2022, **32**, 2207732.
3. K. Zhao, G. Fan, J. Liu, F. Liu, J. Li, X. Zhou, Y. Ni, M. Yu, Y.-M. Zhang, H. Su, Q. Liu and F. Cheng, *Journal of the American Chemical Society*, 2022, **144**, 11129-11137.
4. G. Wang, Q. Dou, P. Xiong, Q. Liu, D. Min and H. S. Park, *Chem. Eng. J.*, 2023, **457**, 141250.
5. J. Wei, P. Zhang, T. Shen, Y. Liu, T. Dai, Z. Tie and Z. Jin, *ACS Energy Lett.*, 2023, **8**, 762-771.
6. G. Zhang, L. Fu, Y. Chen, K. Fan, C. Zhang, H. Dai, L. Guan, H. Guo, M. Mao and C. Wang, *Angew. Chem. Int. Ed.*, 2024, **63**, e202412173.
7. G. Zhang, L. Fu, Y. Chen, K. Fan, C. Zhang, H. Dai, L. Guan, M. Mao, J. Ma and C. Wang, *Adv. Mater.*, 2024, **36**, 2405949.
8. J. Luo, L. Xu, Y. Yang, S. Huang, Y. Zhou, Y. Shao, T. Wang, J. Tian, S. Guo, J. Zhao, X. Zhao, T. Cheng, Y. Shao and J. Zhang, *Nat. Commun.*, 2024, **15**, 6471.
9. M. Yu, J. Mu, L. Wang, Y. Niu, W. Si, J. Li, X. Liu, T. Li, X. Li, W. Zheng, Y. Dai, X. Jiang and G. He, *Energy Environ. Sci.*, 2025, **18**, 1502-1513.
10. Z. Cai, Y. Ou, J. Wang, R. Xiao, L. Fu, Z. Yuan, R. Zhan and Y. Sun, *Energy Storage Mater.*, 2020, **27**, 205-211.
11. Q. Li, H. Wang, H. Yu, M. Fu, W. Liu, Q. Zhao, S. Huang, L. Zhou, W. Wei, X. Ji, Y. Chen and L. Chen, *Adv. Funct. Mater.*, 2023, **33**, 2303466.
12. H. Tang, N. Hu, L. Ma, H. Weng, D. Huang, J. Zhu, H. Yang, Z. Chen, X. Yin, J. Xu and H. He, *Adv. Funct. Mater.*, **n/a**, 2402484.
13. Y. Zhou, G. Li, S. Feng, H. Qin, Q. Wang, F. Shen, P. Liu, Y. Huang and H. He, *Adv. Sci.*, 2023, **10**, 2205874.
14. G. Li, Z. Zhao, S. Zhang, L. Sun, M. Li, J. A. Yuwono, J. Mao, J. Hao, J. Vongsvivut and L. Xing, *Nat. Commun.*, 2023, **14**, 6526.
15. J. Cui, X. Liu, Y. Xie, K. Wu, Y. Wang, Y. Liu, J. Zhang, J. Yi and Y. Xia, *Mater. Today Energy*, 2020, **18**, 100563.
16. H. Yu, Y. Chen, H. Wang, X. Ni, W. Wei, X. Ji and L. Chen, *Nano Energy*, 2022, **99**, 107426.
17. H. Zhang, X. Gan, Z. Song and J. Zhou, *Angewandte Chemie*, 2023, **135**, e202217833.
18. Y. Song, W. Lu, H. Yang, C. Wu, W. Wei, G. Kuang, Y. Chen, L. Chen and X. Ouyang, *Nano Energy*, 2024, **120**, 109094.
19. D. Li, Y. Tang, S. Liang, B. Lu, G. Chen and J. Zhou, *Energy Environ. Sci.*, 2023, **16**, 3381-3390.
20. D. Xie, Y. Sang, D.-H. Wang, W.-Y. Diao, F.-Y. Tao, C. Liu, J.-W. Wang, H.-Z. Sun, J.-P. Zhang and X.-L. Wu, *Angew. Chem. Int. Ed.*, 2023, **62**, e202216934.
21. H. Liu, Z. Xu, B. Cao, Z. Xin, H. Lai, S. Gao, B. Xu, J.-L. Yang, T. Xiao, B. Zhang and H. J. Fan, *Adv. Energy Mater.*, 2024, **14**, 2400318.
22. L. Wang, Z. Zhao, Y. Yao, Y. Zhang, Y. Meng, B. Hu, J. Kang, J. Guo, L. Zhang and H. Lu, *Energy Storage Mater.*, 2023, **62**, 102920.